Fast Reversible Isomerization of Merocyanine as a Tool to Quantify Stress History in Elastomers

Yinjun Chen[1], C. Joshua Yeh[1], Qiang Guo[2], Qi Yuan[2], Rong Long[2] and Costantino Creton[1]*

[1]*Laboratory of Soft Matter Science and Engineering, ESPCI Paris, Université PSL, CNRS, Sorbonne Université, 75005 Paris, France*

[2]*Department of Mechanical Engineering, University of Colorado Boulder, Boulder, CO, USA 80309.*

1. Synthesis of multiple network elastomers and characterization of mechanical properties

1.1 Synthesis of mechanochromic multiple network elastomers

The SP mechanophore was synthesized as previously reported[1] and the detailed procedure is shown in Scheme S1. SP diol was synthesized by the addition reaction of compound of **2** and **3**, and then was functionalized with double bonds via the substitution reaction with methacryloyl chloride. Thus an SP-diene yellow powder was obtained and was used as a crosslinker in the polymerization of multiple network elastomers.

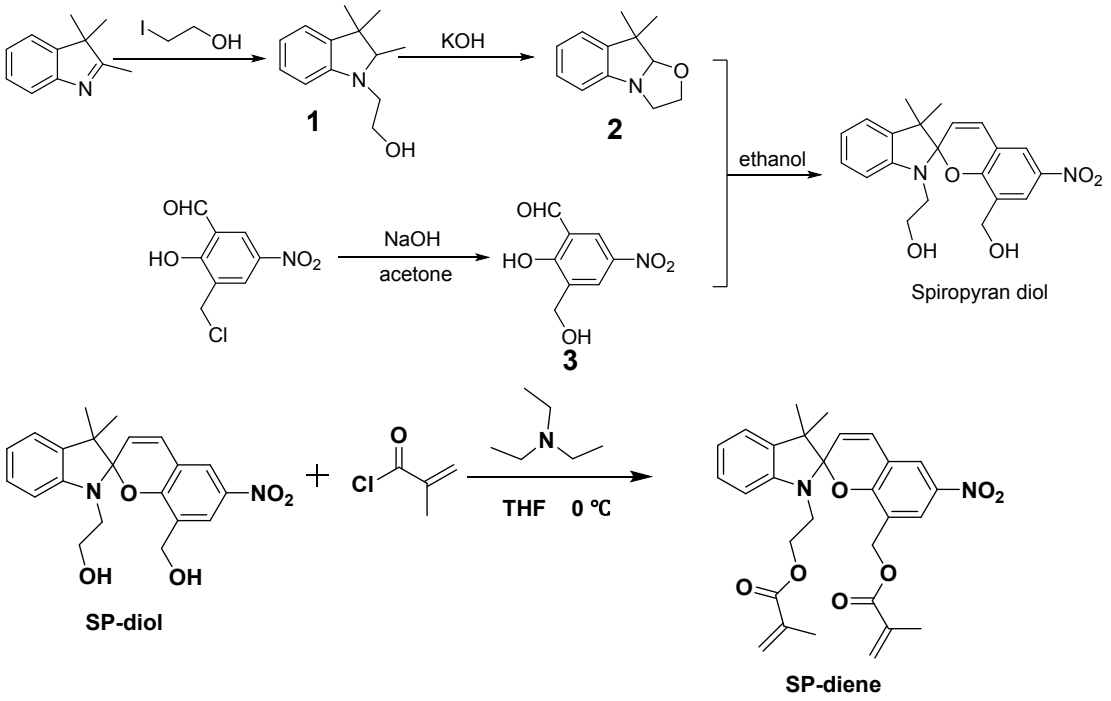

Scheme S1: *The synthesis of the SP crosslinker*

Single network (SN) materials were synthesized in the following way: 0.05 mol% SP and 0.15 mol% 1,4-butanediol diacrylate (BDA) crosslinker (relative to monomer) were dissolved into ethyl acrylate (EA) monomer with 1 mol% 2-hydroxy-2-methylpropiophenone (HMP) photo initiator. The mixture was then poured into a mold composed of a metal scaffold, a silicone spacer and two flat pieces of glass, and then polymerized 2 hours by UV exposure. As previously described[2], the single network acts as a filler network in multiple network elastomers and mainly controls the mechanical properties of the materials. To compare the evolution of the stress in a dynamic deformation process such as fracture for different materials, we also synthesized a different single network by increasing the total crosslinker concentration from 0.2 mol% to 0.5 mol% and keeping a constant SP concentration (0.05 mol%) relative to EA monomer. Using these two SNs as filler networks, varying families of materials were prepared by repeated swelling and polymerization steps with EA monomer. The composition of the matrix is the same as that previously reported with EA monomer and 0.01 mol% crosslinker. All the materials used in this article are shown in Table S1.

Table S1: *Various multiple network elastomers were synthesized for the quantification of stress*

Polymer name	x-linker mol%	SN wt%	C_{SP} mol%	λ_0	N_{poly}
EA0.5-0.05(1)	0.5	100	0.05	1	1
EA0.5-0.05(1.56)EA	0.5	26.5	0.05	1.56	2
EA0.5-0.05(2.23)EA	0.5	9.0	0.05	2.23	3
EA0.2-0.05(1)EA	0.2	4.4	0.05	2.84	1
EA0.2-0.05(1.70)	0.2	100	0.05	1	2
EA0.2-0.05(2.61)EA	0.2	20.2	0.05	1.70	3

x-linker represents the crosslinked density in the filler network of polymer materials. N_{poly}, Csp, and λ_0 are the total step number of polymerization, SP concentration and prestretch in the filler network.

1.2 Uniaxial tensile test

The multiple network elastomers (MNE) in Table S1 were used to perform uniaxial extension tests. Uniaxial extension experiments were performed on a standard tensile Instron machine (model 5565, fitted with a 100 N load cell). Samples with a dog-bone shape were used to carry out elongation tests with a stretch rate $\dot{\lambda} = 0.05\ s^{-1}$ and the stretch was measured with a camera by recording the position of two black marks on the centers of the dog-bone samples. The stress-strain curves for various samples are shown in Figure S1.

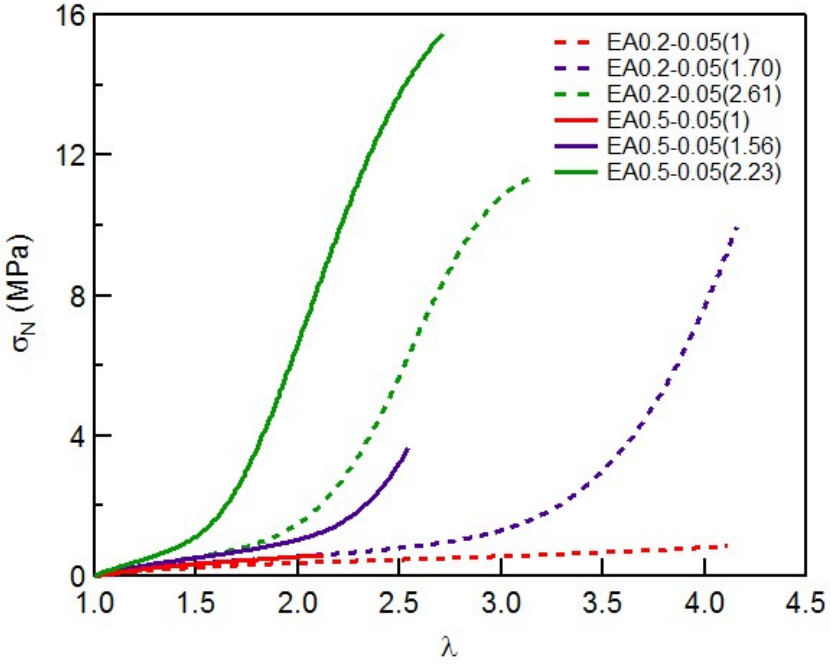

Figure S1: *Stress-strain curves of the EA0.2-0.05 and EA0.5-0.05 families of samples*

1.3 Step cyclic loading

Step cyclic loading were also performed on the EA0.2-0.05(2.61) and EA0.5-0.05(2.23) materials with a nominal stretch rate of 0.05 s^{-1}. The maximum strains λ ranged from 1.5 to 2.8 and the maximum stretch increased by 0.1 at every step as shown in Figure S2. An RGB camera (SENTECH: STC-MCS241U3V, Image sensor: SONY IMX174, cell size: $5.86\,\mu m \times 5.86\,\mu m$) was used to record the color change of the samples in step cyclic loading tests. All the frames extracted from the videos were used to do RGB analysis.

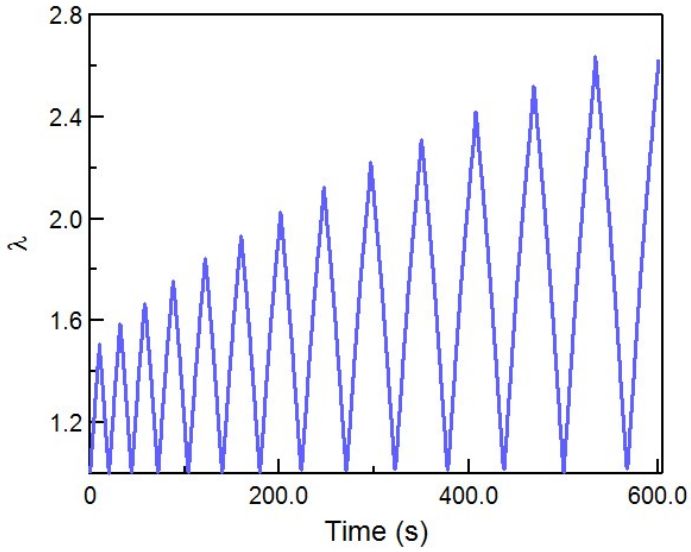

Figure S2: *Stretch as a function of time during a step-cyclic loading test. The maximum stretch value of each cycle increased with each cycle by 0.1.*

Figure S3a shows the stress-strain curves of EA0.5-0.05(2.23) and EA0.2-0.05(2.61). Both materials exhibit an obvious Mullins effect and a low viscoelasticity. When the stretch λ increases to λ = 1.8, the EA0.5-0.05(2.23) samples start to show an obvious hysteresis, validating the initiation of damage in the material. Accumulated hysteresis is calculated in step cyclic loading tests and shown in Figure S3b.

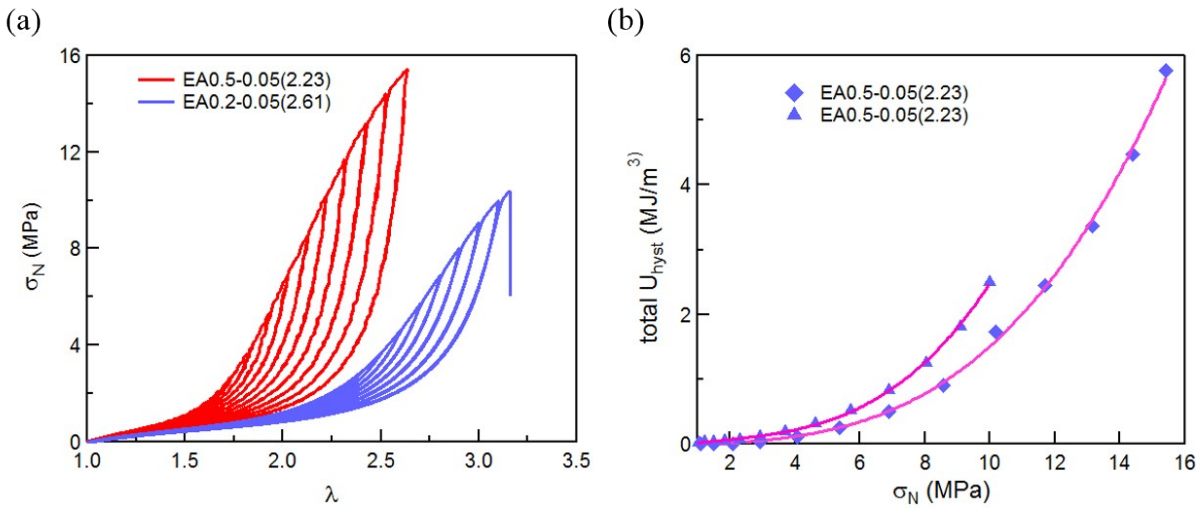

Figure S3: *Mechanical properties of EA0.5-0.05(2.23) and EA0.2-0.05(2.61) samples. (a) Stress-strain curve; (b) Accumulated hysteresis in step cyclic loading test.*

2. Color analysis

2.1. Image processing

Color correction and image processing applied to each video frame was carried out by using the same protocol outlined in the previous report[2].

2.2. Chromaticity

Chromaticity from color theory was used to quantify the color state of a pixel. The chromaticity of a channel in a pixel is defined as:

$$S_{ratio} = \frac{S}{\sum S}, \tag{S1}$$

where S is the generic representation of a color channel (R, G, or B). Chromaticity represents the relative contribution of a color channel relative to the total pixel intensity. The change in chromaticity, ΔS_{ratio}, relative to the beginning of an experiment can be tracked for each pixel and correlated with the applied nominal stress. Based on the chromatic changes for each color channel, the total color change, ΔT_{ratio}, can be defined as the Euclidean norm:

$$\Delta T_{ratio} = \sqrt{\sum \Delta S_{ratio}^{2}}. \tag{S2}$$

Note that the color state of a pixel is sufficiently described by two chromatic descriptors, since the other chromatic descriptors can be determined based on Eq. (S1) and Eq. (S2).

2.3. Construction of the color-stress calibration map

The chromatic change of each color channel during a step-cyclic loading test of an EA0.2-0.05(2.61) sample can be visualized as a function of time in Figure S4a and as a function of nominal stress in Figure S4b. Specific chromatic descriptors (Total Chromatic change $^{\Delta T_{ratio}}$ and green chromatic change $^{\Delta G_{ratio}}$) were chosen for the stress-color map based on their high sensitivity for the loading and unloading step, respectively. Figure S5 shows the change in these chromatic descriptors during loading (blue line) and unloading from a specific maximum load (red lines). The loading of a virgin sample determines the level of SP activation into MC and during unloading and reloading, the chromatic coordinates retrace the same path, implying that the color change during unloading and reloading is a reversible process. If the chromatic change is plotted as a function of nominal stress, the red and blue chromatic changes do not show any obvious variation when the nominal stress is above 2.5 MPa in unloading and reloading. However, the green chromatic change rapidly decreases with nominal stress during unloading and increases during reloading as show in Figure S4b.

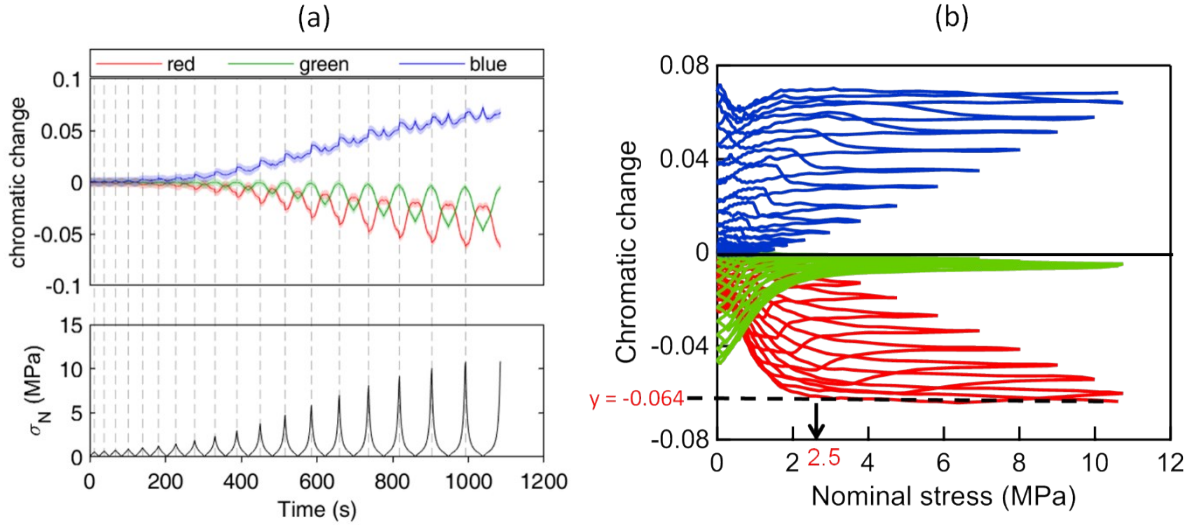

Figure S4: *(a) The red, green, and blue chromatic changes of an EA0.2-0.05(2.61) sample undergoing step cyclic loading. The top and bottom figures share the same time axis. Dashed lines correspond to peak stress along the time axis. The transparent shaded regions in the*

chromatic change evolution correspond to one standard deviation. (b) Red, Green and Blue chromatic changes as a function of nominal stress in step cyclic loading-unloading tests. The zero line (black solid line) corresponds to the initial color of the sample after correction of the background. The black dotted line at y= -0.064 and intersects the red chromatic change curve at the nominal stress above 2.5 MPa.

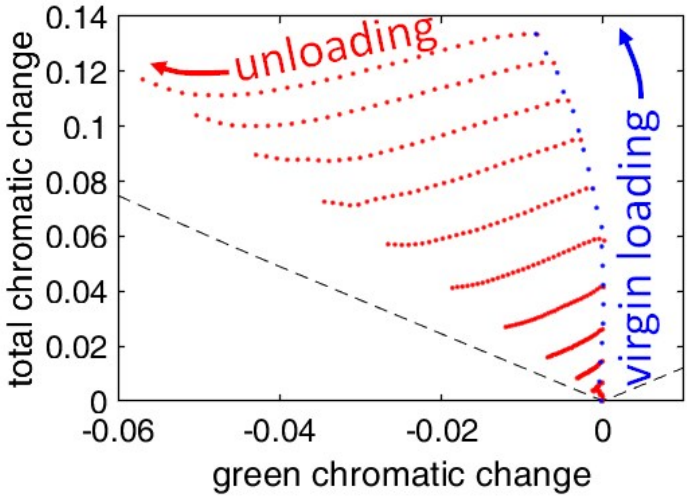

Figure S5: *Chromatic map of an EA0.2-0.05(2.61) sample undergoing step cyclic loading. Blue dots represent measured chromatic changes while the sample was undergoing its first loading. Red dots represent measured chromatic changes while the sample was unloading and reloading. The dashed line corresponds to the boundary of physical meaningful chromatic coordinates.*

A third order polynomial fit,

$$f(x) = p_1x^3 + p_2x^2 + p_3x + p_4, \quad \text{(S3)}$$

was used to describe the chromatic unloading paths obtained experimentally, as shown in Figure S6. The polynomial fit was performed using a total least-squares fitting method, in which the Euclidean distance between the experimental datapoints and the fitted line was minimized. This fitting approach accounts for variances in both the total chromatic and green chromatic changes. Also, to aid the interpolated prediction of unloading chromatic traces for a given applied peak stress, the polynomial fit was based on a normalized green chromatic change:

$$(\Delta G_{ratio})_{norm} = \frac{(\Delta G_{ratio}) - (\Delta G_{ratio})_{avg}}{(\Delta G_{ratio})_{std}}, \quad \text{(S4)}$$

where the subscripts, avg and std, denote the average and standard deviation of the experimental green chromatic change.

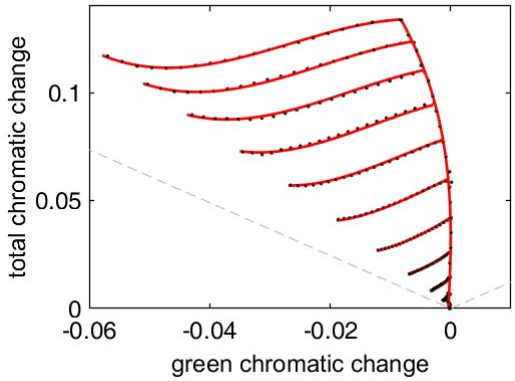

Figure S6: *Chromatic map of an EA0.2-0.05(2.61) sample undergoing step cyclic loading. The black dots represent experimental datapoints. The grey dashed line corresponds to the boundary of physically meaningful chromatic coordinates. The solid red lines represent a third order polynomial fit based on a normalized green chromatic change.*

To predict the unloading trace for a given peak stress along the loading curve, the third order polynomial coefficients used to fit the measured unloading chromatic curves were interpolated based on a fourth order polynomial fit as a function of the normalized green chromatic change when the sample was completely unloaded, as shown in Figure S7. Note that interpolation was not performed as a function of a given peak stress along the loading curve, since the peak stress of a pixel is not known a priori. Once the interpolated fitting coefficients were determined, the corresponding normalized green chromatic change was generated by spline interpolation of $(\Delta G_{ratio})_{avg}$ and $(\Delta G_{ratio})_{std}$ as a function of the green chromatic change of the completely unloaded sample, as shown in Figure S8. The interpolated fitting coefficients (p_1, p_2, p_3, and p_4) and interpolated $(\Delta G_{ratio})_{avg}$ and $(\Delta G_{ratio})_{std}$ were used to construct the predicted unloading chromatic curves as shown in Figure S9.

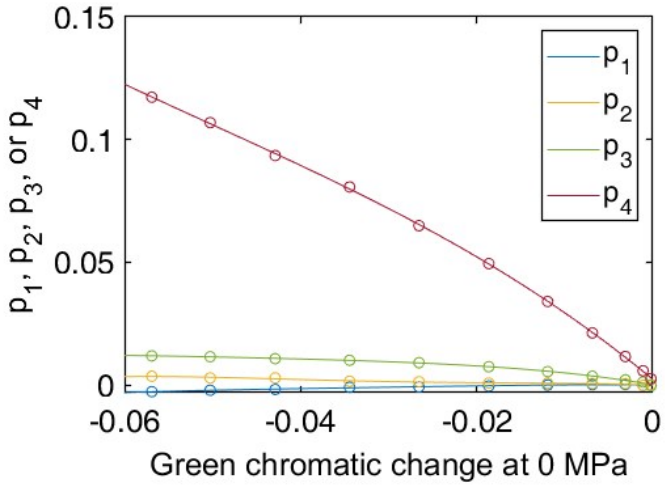

Figure S7: *A fourth order polynomial fit of the third order polynomial fitting coefficients used to fit the experimental datapoints obtained from an EA0.2-0.05(2.61) sample undergoing step cyclic loading (see Figure 3). The fitting coefficients,* p_1, p_2, p_3, *and* p_4 *correspond to the coefficients in Eq. (S3).*

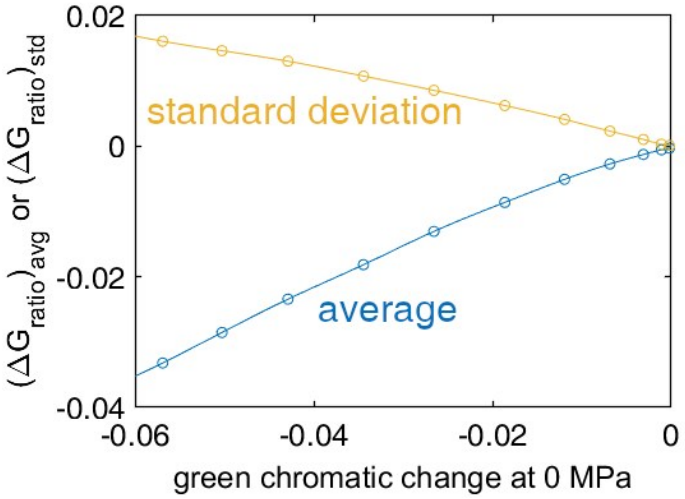

Figure S8: *Spline interpolation of the average and standard deviation of the normalized green chromatic change (see Eq. (S4).*

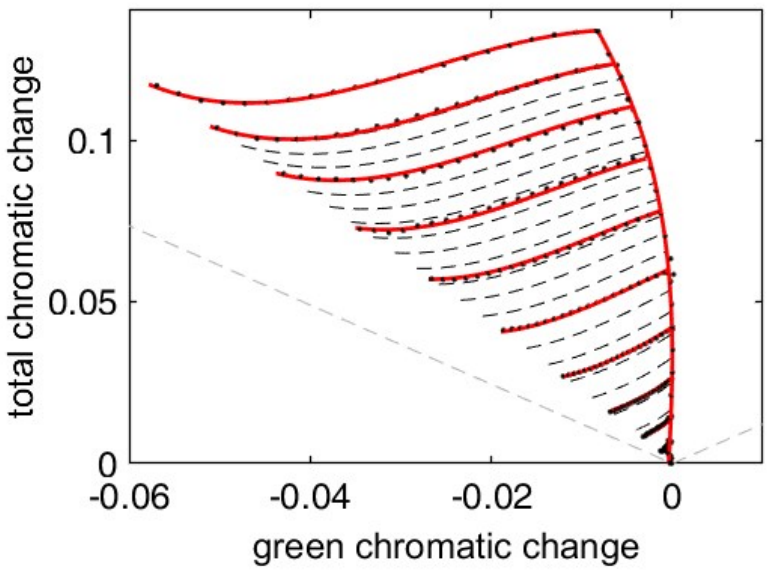

Figure S9: *Chromatic map of an EA0.2-0.05(2.61) sample undergoing step cyclic loading. The black dots represent experimental datapoints. The solid red lines represent a third order polynomial fit based on a normalized green chromatic change. The black dashed lines are interpolated unloading chromatic traces. The grey dashed line corresponds to the boundary of physical meaningful chromatic coordinates.*

The chromatic map in Figure S5 can be correlated to the applied nominal stress by overlaying isostress lines, as shown in Figure S10. To accomplish this, the unloading chromatic traces were fitted with the applied nominal stress, creating a 3D fit in the $^{\Delta T_{ratio}}\_^{\Delta G_{ratio}}\_^{\sigma_N}$ space that can be used to interpolate the corresponding chromatic coordinates based on a prescribed nominal stresses. Isostress lines were created by fitting a smoothing spline to the chromatic coordinates for each level of stress.

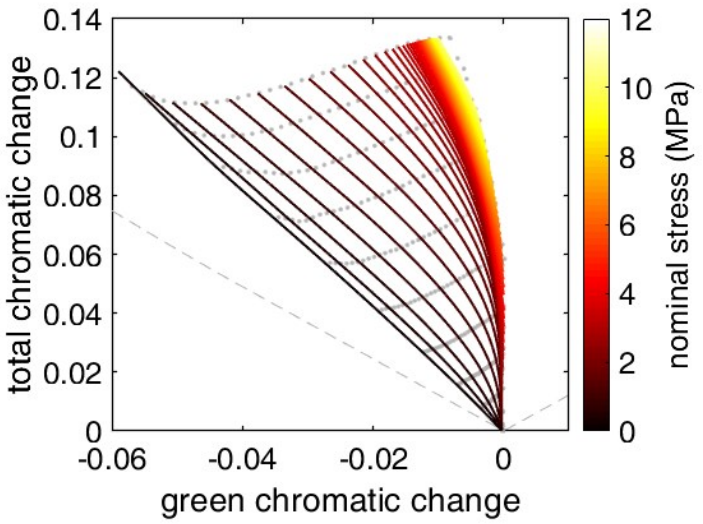

Figure S10: *Chromatic-stress map of an EA0.2-0.05(2.61) sample undergoing step cyclic loading. Grey dots represent experimental datapoints (see Figure S5). Isostress lines are represented by colored solid lines that correspond to the color bar on the right. The dashed line marks the boundary of physically meaningful chromatic coordinates.*

Application of the chromatic stress calibration map (3D color-stress map)

The dynamic process of crack propagation was taken as an example for the application of the chromatic stress calibration map. A flow chart summarizing how the stress is mapped and the peak stress is calculated are depicted in Figure S11.

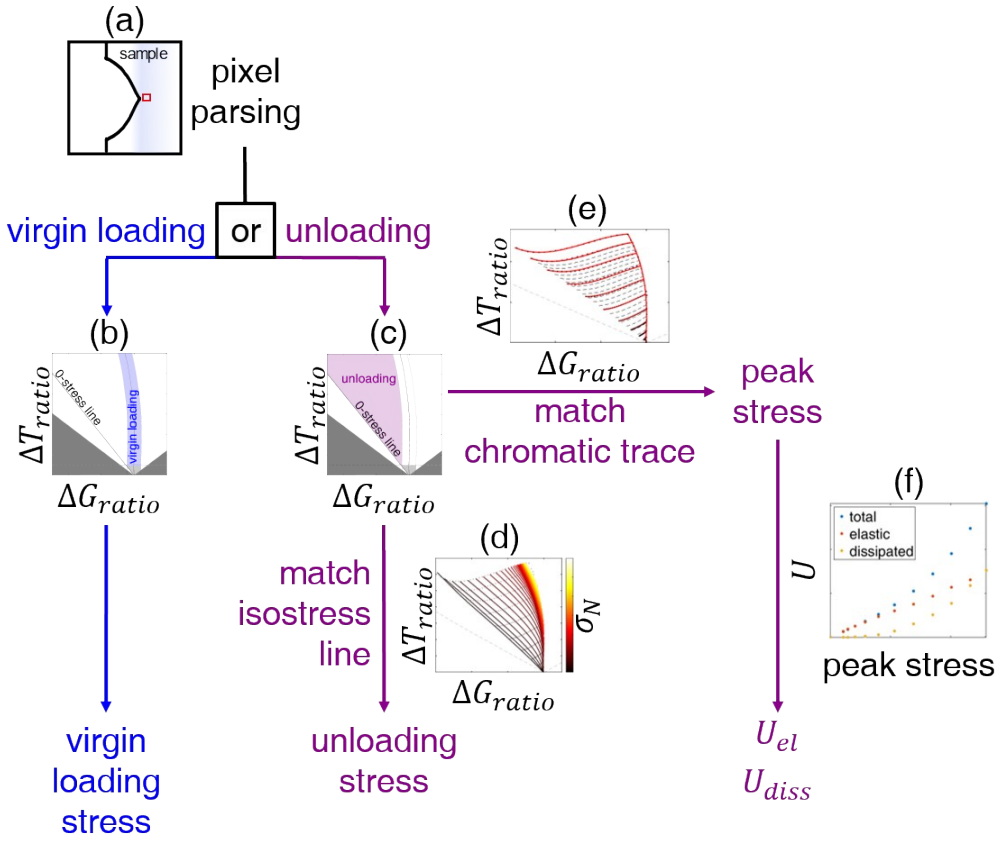

Figure S11: *A diagram of how the images taken from the sample are analyzed. (a) A pixel in the sample region is selected for analysis. The pixel is parsed as virgin loading (b and Figure S13) or unloading (c and Figure S13)). Pixels parsed as unloading are associated with an unloading stretch by matching an unloading isostress line (d and Figure S10)). Also, unloading pixels are matched with an unloading chromatic trace (e and Figure S9) so that the peak nominal stress can be determined. The nominal peak stress is used to determine the elastic energy density,* U_{el}*, and the dissipated energy density,* U_{diss}*, by using a calibration curve (f and Figure S14))*

Consider a rectangular, single edge notched fracture sample, in which the sample is pulled to failure. At the beginning of the experiment, a representative sample region in the image frame is used to estimate noise associated with sample surface roughness, surface impurities, etc. By observing histograms of the chromatic changes for each color channel and the total chromatic change in this region, as shown in Figure S12, a threshold value based on the 95% and 5% percentile of the total and green chromatic change, respectively, was established to differentiate signal from noise. The noise thresholds are also plotted on the chromatic map in Figure S13.

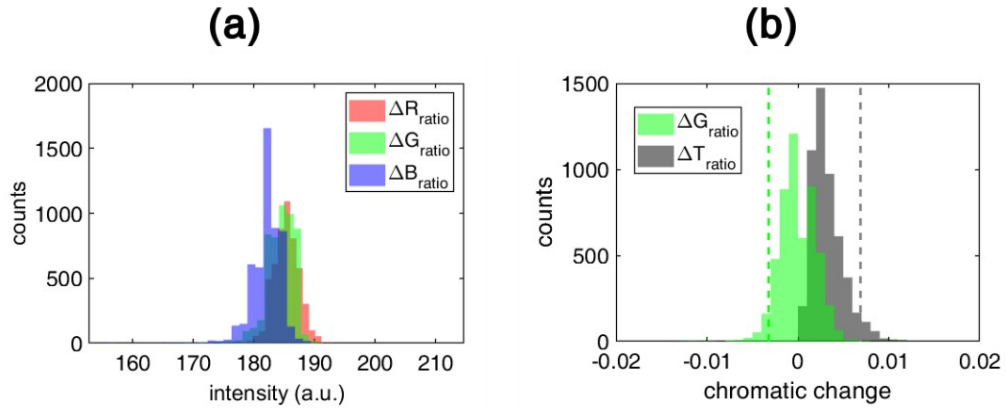

Figure S12: *(a) Histograms of chromatic changes for each color channel. (b) Histograms of the total and green chromatic changes. The green and black dashed lines represent the 5% and 95% percentile in the green and total chromatic change distribution.* $^{\Delta G_{ratio}}$ *and* $^{\Delta T_{ratio}}$ *pairs that fall within the dashed lines were labelled as noise. Histograms were generated from the same representative sample region prior to loading.*

As the fracture sample is stretched, the sample color and crack geometry will begin to change. A masking protocol (to mask the void created by the open crack) was used as described in Chen et al[2] . Briefly, the image frame was guided by a binary thresholding method and subsequently modified manually, so that the front facing area of the sample was analyzed and that sample defects and regions exhibiting tri-dimensionality were ignored. The additional masking ensures that analysis is limited to regions where the sample thickness is relatively homogeneous.

Chromatic coordinates of the analyzed sample region are mapped onto the chromatic stress calibration map and are subsequently parsed as being under virgin loading or unloading, as shown in Figure S13. The boundaries used to parse the chromatic data were based on the absolute value of the 5% percentile of $^{\Delta G_{ratio}}$ of a representative sample region at the beginning of the experiment, herein referred to as $^{\sigma_{\Delta G_{ratio}}}$. The virgin loading region was defined by shifted loading curves along

the x-axis by $\pm \sigma_{\Delta G_{ratio}}$. Datapoints that fall to the right threshold boundary were discarded in the analysis. Datapoints located in the purple region in Figure S13 were identified as pixels undergoing unloading and were associated with an unloading chromatic trace (see Figure S9) and an unloading isostress line (see Figure S10). Data falling within the blue region in Figure S13 were counted as pixels undergoing virgin loading and were correlated with a stress level along the virgin loading curve. Data association for virgin loading and unloading were performed using a MATLAB built-in function, knnsearch, which is a nearest neighbor algorithm.

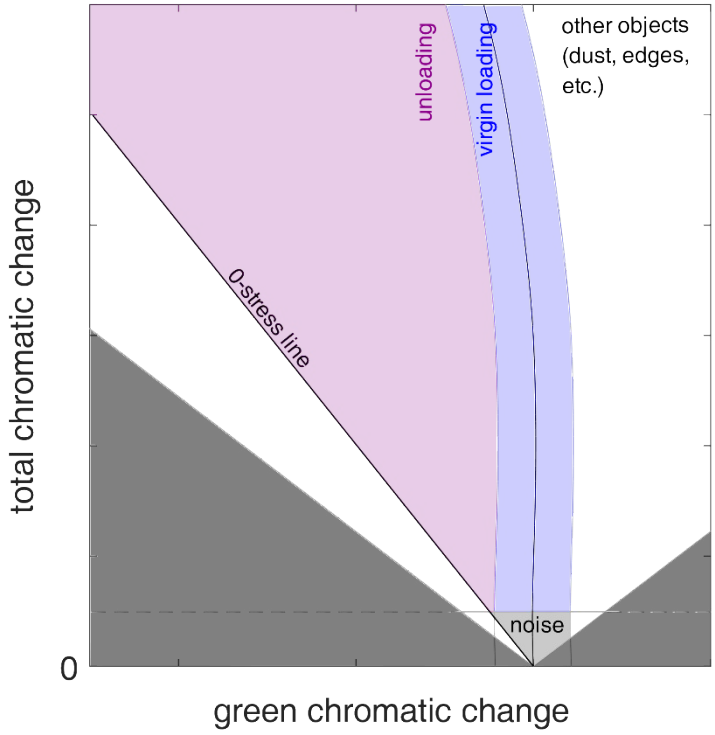

Figure S13: *A schematic of how chromatic datapoints are parsed as virgin loading (blue region) or unloading (purple region). The white and light grey regions associated with noise, background, etc. were excluded from the analysis. The quasi-vertical grey lines that define the boundaries of the virgin loading region. The horizontal grey line marks the 95% percentile in the total chromatic change distribution prior to sample loading (see Figure S12b). The diagonal black line traces the isostress line when then same was completely unloaded. The dark grey areas represent unphysical chromatic coordinates.*

For pixels matched with an unloading chromatic trace on the chromatic stress map, information on the loading history was deduced, such as the peak nominal stress, elastic energy density, and dissipated energy density. The peak nominal stress was determined by finding the intersection between the unloading and virgin chromatic traces. Based on the peak nominal stress, the

associated elastic and dissipated energy density was calculated from the stress-strain data of the step-cyclic loading experiment in uniaxial extension, as shown in Figure S14.

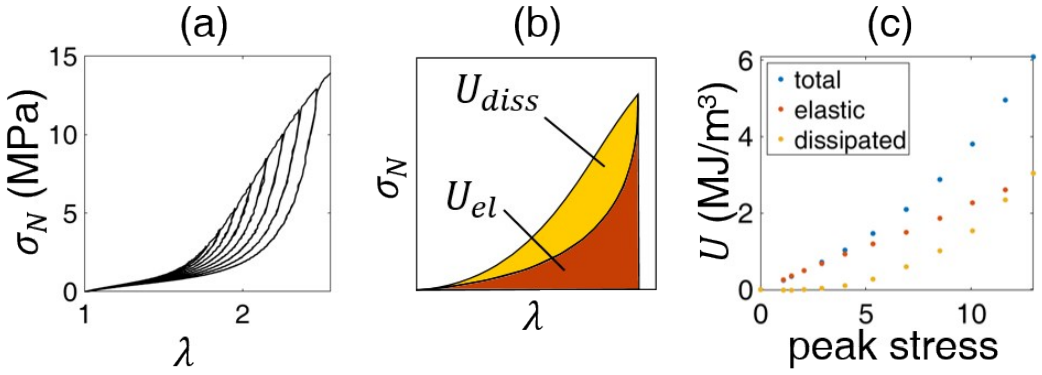

Figure S14: *(a) Nominal stress and extension of a step cyclic loading test. (b) A schematic showing that the dissipated and elastic energy density is determined from the area between the loading-unloading curve and the area under the unloading curve, respectively. (c) A calibration curve between the total, elastic, or dissipated energy density and the peak nominal stress.*

3. Post mortem analysis

Post mortem samples were obtained by carrying out a fracture test on a rectangular sample (5 mm wide, ~2 mm thick) with a single edge notch (~0.5 mm). The sample failed into two separate parts, which were used for color analysis. Based on the color change as a function of distance perpendicular from the crack edge, the stress history and concentration of activated mechanophore was determined.

3.1. Energy densities based on total color change

The peak stress, and energy densities (elastic and dissipated) were associated with the measured total chromatic change at 0-stress, $^{\Delta T}{}_{ratio}^{\circ}$, for each cycle taken from the step cyclic loading test. Calibration curves for both EA0.5-0.05(2.23) and EA0.2-0.05(2.61) are shown in Figure S15 and Figure S16, respectively. A linear fit was used to describe the correlation between the peak nominal stress and $^{\Delta T}{}_{ratio}^{\circ}$, elastic energy density ($^{U}{}_{el}$) and $^{\Delta T}{}_{ratio}^{\circ}$. To describe the correlation between the dissipated energy density, $^{U}{}_{diss}$, and $^{\Delta T}{}_{ratio}^{\circ}$, a 4th order polynomial fit was used. To account for errors in both the measured $^{\Delta T}{}_{ratio}^{\circ}$ and peak stress or energy density, a total least squares approach that minimizes the orthogonal distance between the datapoints and the fit was used.

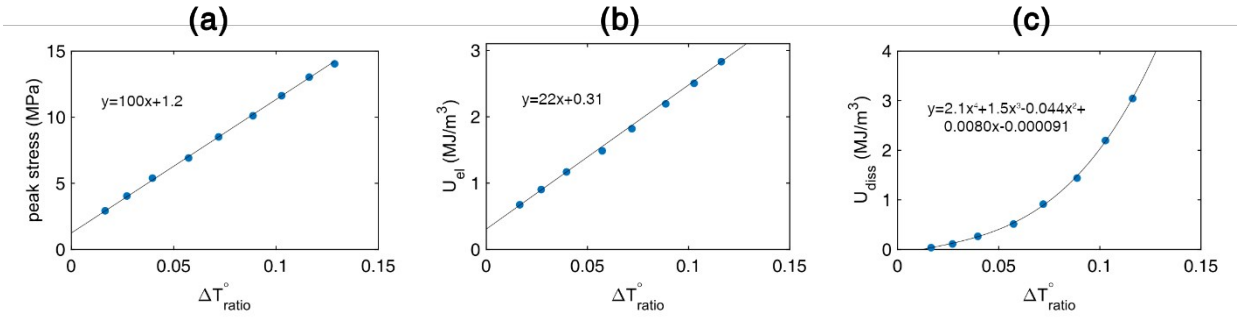

Figure S15: *Calibration curves relating the peak nominal stress (a), elastic energy density, U_{el}, (b), and the dissipated energy density, U_{diss}, (c) to ΔT°_{ratio} for an EA0.5-0.05(2.23) sample.*

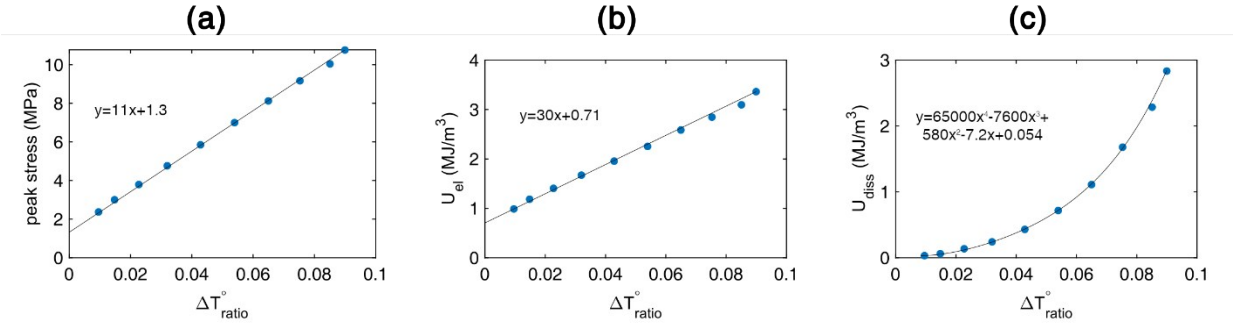

Figure S16: *Calibration curves relating the peak nominal stress (a), elastic energy density, U_{el}, (b), and the dissipated energy density, U_{diss}, (c) to ΔT°_{ratio} for an EA0.2-0.05(2.61) sample.*

4. Stress maps

4.1 Maps of stress above 3 MPa

Stress maps around the crack tip were quantified by using the 3D color-stress map. In uniaxial step cyclic loading tests, when the stress increased to 3 MPa, the materials presented an obvious total hysteresis. In those materials, the irreversible hysteresis measured in uniaxial extension represents the damage in the polymer networks. Thus the regions where the stress exceeded 3MPa was mapped around the crack tip as shown in Figure S17. Before crack propagation the high stress almost concentrates in an area close to the crack tip, but during the slow advance of the crack the high stress region expands to the area far from the crack tip.

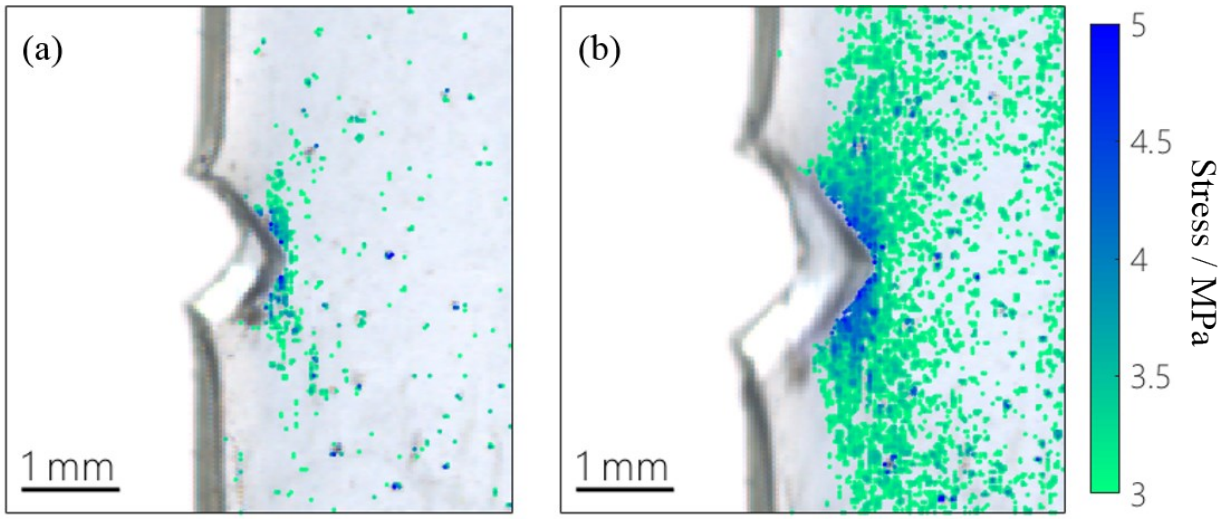

Figure S17: *Stress map around the crack tip of EA0.5-0.05(2.23) samples before and during crack propagation.*

4.2 Initiation of crack propagation

Before failure, materials with a notch normally display a slow and small advance of the crack followed by a rapid propagation resulting in the failure of materials. The color change of the materials around the crack tip during the slow advance stage are shown in Figure S18. From Figure S18 (a) to (f) it is observed that the crack surface increases gradually during the slow advance stage. The Figure S18 (a) and (f) are respectively corresponding to the original position of the slow and rapid propagation. In Figure S18 two small purple regions (partially unloaded) are symmetrically located near the crack tip. The evolution of stress distribution around the crack tip was quantified by using the 3D color-stress map. Figure S19 shows that the stress map evolution around crack tip prior to and during crack propagation.

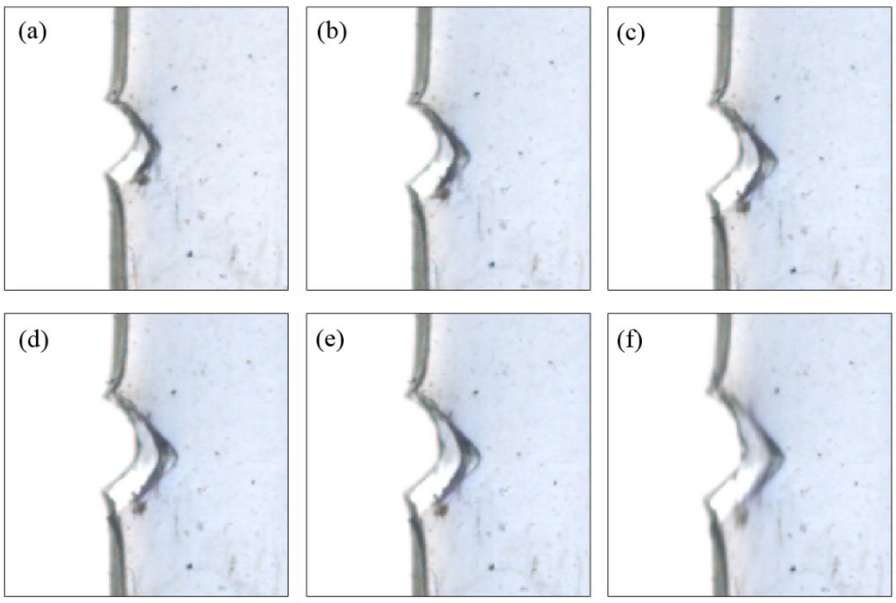

Figure S18: *Original images of EA0.5-0.05(2.23) sample with a notch during the crack propagation*

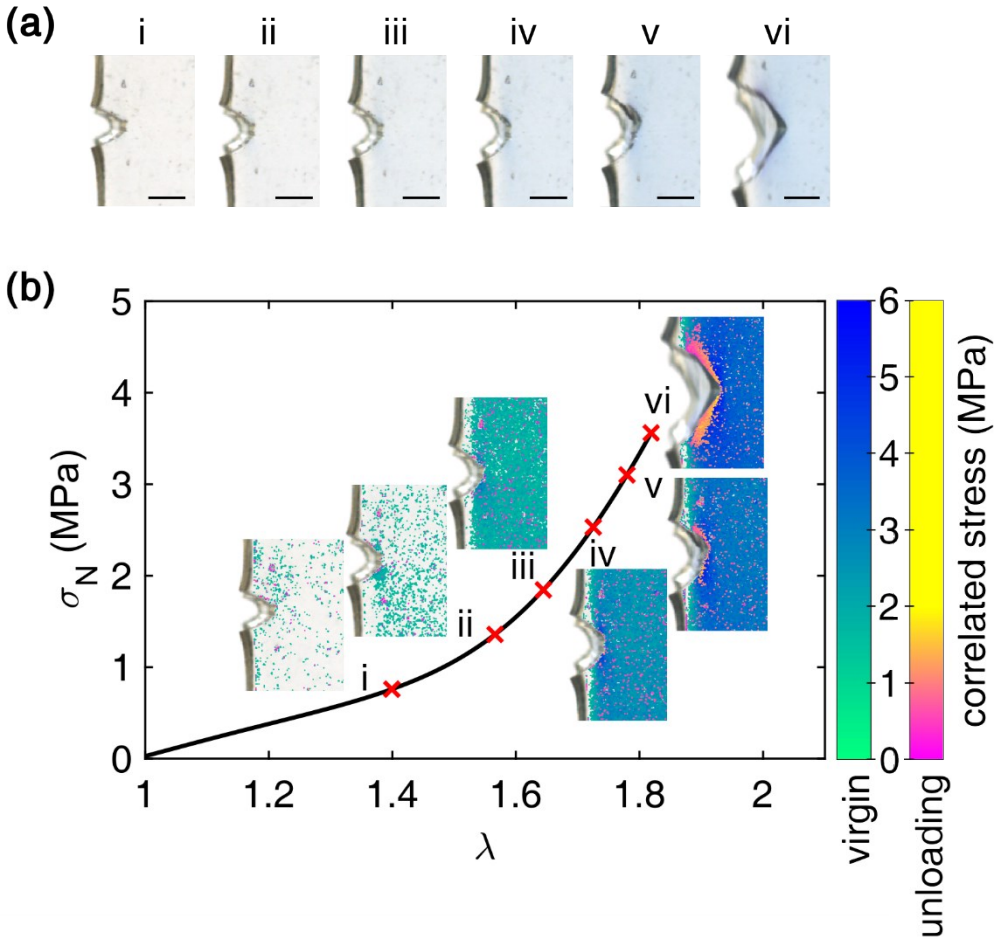

Figure S19: *Stress maps of EA0.5-0.05(2.23) sample with a notch during the crack propagation. (a) The original images of EA0.5-0.05(2.23) sample with a single-edge notch showing two different color changes during a fracture test. The sample color changes from colorless to blue around the crack tip prior to the propagation and then some regions change from blue to purple during the crack propagation. The scale bar in the images represents 0.5 mm. (b) The stress map evolution is shown in (b).*

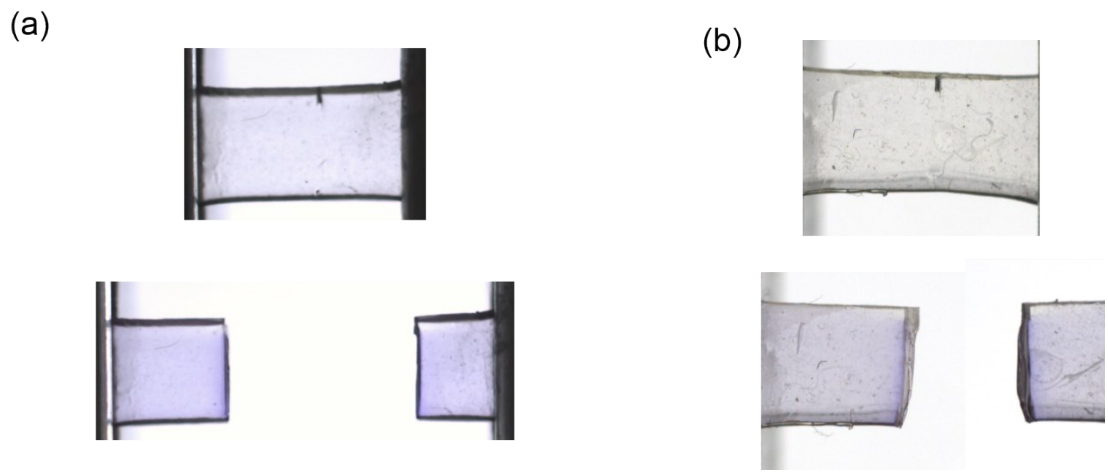

Figure S20: *Images of (a) EA0.5-0.05(2.23) and EA0.2-0.05(2.61) samples before and after fracture tests.*

Finite element simulation of crack propagation

An FE model to simulate the crack propagation in the SEN sample was built using the software ABAQUS (version 2019, Simulia, Dassault Systèmes, Providence, RI). The model consists of three main components: i) geometry, i.e., dimensions, mesh and boundary conditions; ii) constitutive model to capture the nonlinear, hysteretic stress-strain relations in the elastomer; iii) cohesive zone model on the projected path of crack propagation. These three components are detailed in the following.

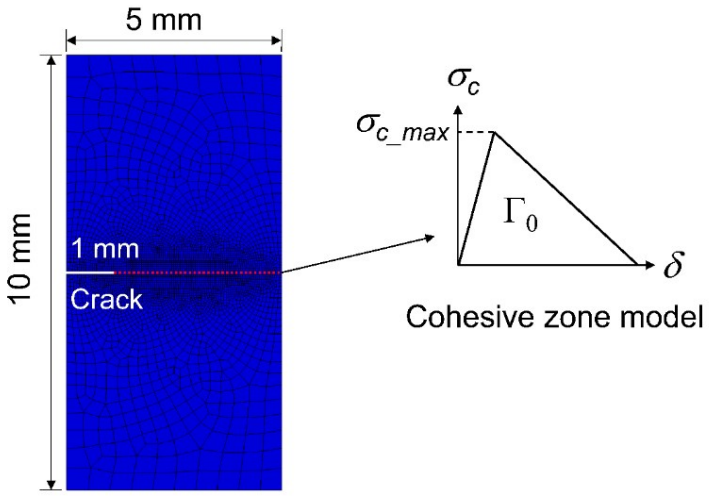

Figure S 21: *FE model for simulating crack propagation in the SEN sample. A cohesive zone model with bilinear traction-separation law was implemented on the projected crack path (directly ahead of the original crack tip).*

5.1 Model geometry

Dimensions of the FE model was set to be the same as the SEN sample (i.e. 5 mm × 10 mm), as shown in Fig. S21. A 1mm crack was introduced on the left side of the model according to the experimental set up. To simulate crack propagation, a cohesive zone was introduced along the projected crack propagation path directly ahead the original crack tip. The top and bottom boundaries were separated by a displacement Δ along the vertical direction, and were subjected to zero displacement along the horizontal direction. The other boundaries (i.e., initial crack surfaces, the left boundary and the right boundary) were set to be traction free. Since the thickness of the SEN sample was much smaller than its lateral dimensions, we meshed the two-dimensional (2D)

FE model using plane stress elements (CPS4R). The mesh near the crack path were refined to improve accuracy with the smallest element size being 0.05 mm. Experimental observation suggested that crack propagation became unstable once the peak load was reached, which would lead to convergence difficulties for the implicit solver based on iterations. Therefore, the simulation was carried out using the explicit dynamic solver (ABAQUS/Explicit).

5.2 Constitutive model

The strain softening behavior of EA0.2-0.05(2.61), as shown in Fig. 2a of the main text, resembles the Mullins effect in filled rubber, which has been extensively studied in the literature. To quantitatively model the nonlinear inelastic behavior, we followed a phenomenological approach that uses one or more internal variables to capture the damage evolution under increasing strain[3-6]. First, we adopted the incompressible Arruda-Boyce model[7], where the nominal stress tensor $\boldsymbol{\sigma}$, also known as the first Piola-Kirchhoff stress tensor in the continuum mechanics literature, was given by the following equation:

$$\boldsymbol{\sigma} = \frac{\mu}{3}\frac{\sqrt{N}}{\lambda_{ch}} L^{-1}\left(\frac{\lambda_{ch}}{\sqrt{N}}\right)\mathbf{F} - p\mathbf{F}^{-T} \ , \qquad \text{(S5)}$$

where μ is the shear modulus at infinitesimal deformation, N is the average number of Kuhn segments on a chain, λ_{ch} is the equivalent stretch ratio on a chain, L^{-1} denotes the inverse Langevin function, $\mathbf{F}$ is the deformation gradient tensor, and p is the Lagrange multiplier to enforce the incompressibility constraint. The equivalent chain stretch λ_{ch} was related to the macroscopic principal stretch ratios, λ_1, λ_2 and λ_3, through the 8-chain model:

$$\lambda_{ch} = \sqrt{\frac{\lambda_1^2 + \lambda_2^2 + \lambda_3^2}{3}} \, . \qquad \text{(S6)}$$

In addition, we applied the following approximation by Cohen[8] for the inverse Langevin function:

$$L^{-1}(y) = y\frac{3 - y^2}{1 - y^2} \, . \qquad \text{(S7)}$$

Under uniaxial tension, Eqs. (S5) and (S6) are reduced to

$$\sigma = \frac{\mu}{3}\frac{\sqrt{N}}{\lambda_{ch}} L^{-1}\left(\frac{\lambda_{ch}}{\sqrt{N}}\right)\left(\lambda - \frac{1}{\lambda^2}\right), \qquad \text{(S8)}$$

and

$$\lambda_{ch} = \sqrt{\frac{\lambda^2 + 2/\lambda}{3}}. \qquad \text{(S9)}$$

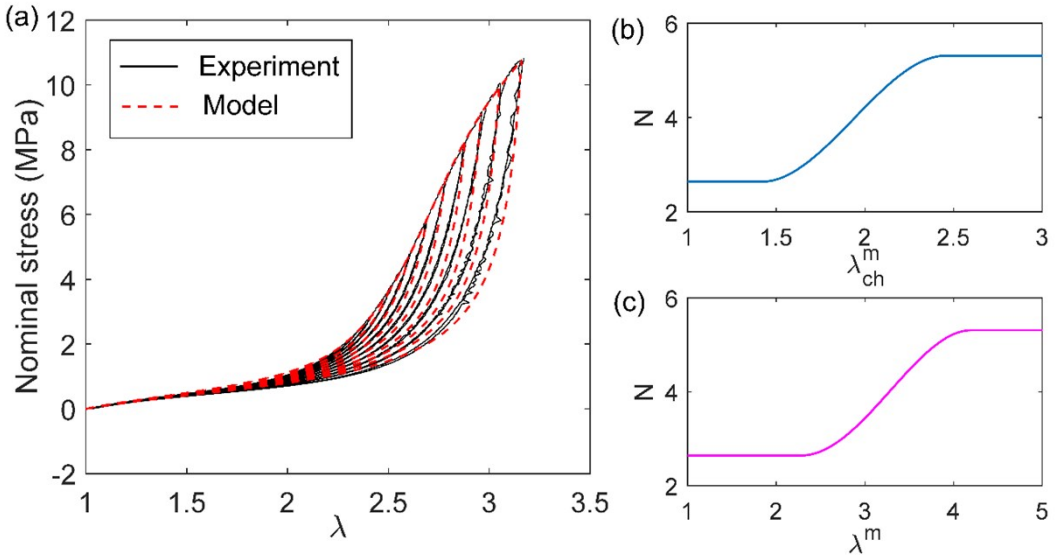

Figure S 22: *Constitutive model for EA0.2-0.05(2.61). (a) Fitting the cyclic tension data using the constitutive model. (b-c) Evolution of the internal N with (b) the maximum equivalent chain stretch experienced in the history* λ_{ch}^m *and (c) the maximum stretch ratio experienced under uniaxial tension* λ^m.

In the Arruda-Boyce model, N is a material constant capturing the finite extensibility of the material. Here we treated N as an internal variable and allowed it to evolve with the loading history. Specifically, N was assumed to be a function of the maximum equivalent chain stretch experienced by the material, denoted as λ_{ch}^m (≥ 1). The second law of thermodynamics dictates that N must be a non-decreasing function with λ_{ch}^m, otherwise it may result in negative energy dissipation over a loading cycle. By fitting the cyclic tension data of EA0.2-0.05(2.61) (see Fig.S22a), we found that $\mu = 0.3$ MPa and the following empirical function for $N(\lambda_{ch}^m)$:

$$N = \begin{cases} 2.64 & 1 \leq \lambda_{ch}^m < 1.45 \\ -4.82817\left(\lambda_{ch}^m - 1\right)^3 + 13.5749\left(\lambda_{ch}^m - 1\right)^2 - 8.8499\left(\lambda_{ch}^m - 1\right) + 4.32 & 1.45 \leq \lambda_{ch}^m < 2.45 \\ 5.31 & 2.45 < \lambda_{ch}^m \end{cases}.$$

(S10)

As illustrated in Fig.S22b, N monotonically increases with λ_{ch}^{m} when $1.45 \leq \lambda_{ch}^{m} < 2.45$. The underlying physical mechanism is that damage in the swollen filler network (e.g. by chain scission) leads to an increase in the overall extensibility (i.e. increased N). Below the lower threshold ($\lambda_{ch}^{m} = 1.45$), damage is negligible and the material is elastic. Beyond the higher threshold ($\lambda_{ch}^{m} = 2.45$), the filler network is fully damaged and N no longer evolves. Under uniaxial tension, there is a one-to-one correspondence between λ_{ch}^{m} and the maximum stretch ratio experienced by the material: λ^{m}. Therefore, N can also be plotted as a function of λ^{m} in Fig.S22c, showing that the material model is elastic when $\lambda^{m} < 2.34$ and becomes inelastic when λ^{m} exceeds 2.34. The constitutive model described above was implemented in the FE simulation through a user subroutine VUMAT, i.e. a Fortran code specifying the stress-strain relations.

5.3 Cohesive zone model

We adopted a bilinear traction-separation law for the cohesive zone model as illustrated in Fig. S21a, and implemented in the FE model by introducing a layer of cohesive elements on the projected crack path (i.e. directly ahead of the crack tip). Since the crack propagation in the SEN sample was in Mode-I, the traction-separation law was in terms of the normal cohesive stress σ_c and the normal gap δ between the crack surfaces. Note that to accommodate the nonlinear effects due to large deformation, σ_c was defined as the normal nominal stress perpendicular to the crack path. The bilinear traction-separation law can be fully specified by three parameters: the intrinsic fracture energy Γ_0 (area enclosed by the traction-separation curve), the cohesive strength σ_{c_max} (maximum stress), and the initial stiffness K. Previous works in the literature[9-10] suggested that the stiffness K did not affect the crack propagation simulation as long as it was sufficiently large. On the other hand, the simulation was sensitive to Γ_0 and σ_{c_max}. We leveraged the data of post-mortem analysis to determine these two parameters.

First, post-mortem analysis showed that the peak nominal stress near the crack surface was about 10MPa (see Fig.4c of the main text). This value was close to the nominal stress at break σ_m under macroscopic tension for EA0.2-0.05(2.61) (i.e., 11.3 MPa as listed in Table 1). The slight difference between the two values (i.e. 10 MPa versus 11.3 MPa) was attributed to the image resolution in the post-mortem analysis, since it posed a limitation accessing material points in the

vicinity of the crack surface. Therefore, the cohesive strength σ_{c_max} was set to be 11.3 MPa. Correspondingly, the initial stiffness K was set to be 8000 MPa/mm, which is sufficiently large since the separation δ related to the cohesive strength σ_{c_max} was only 1.3 μm, much smaller than the smallest element size (= 0.05 mm).

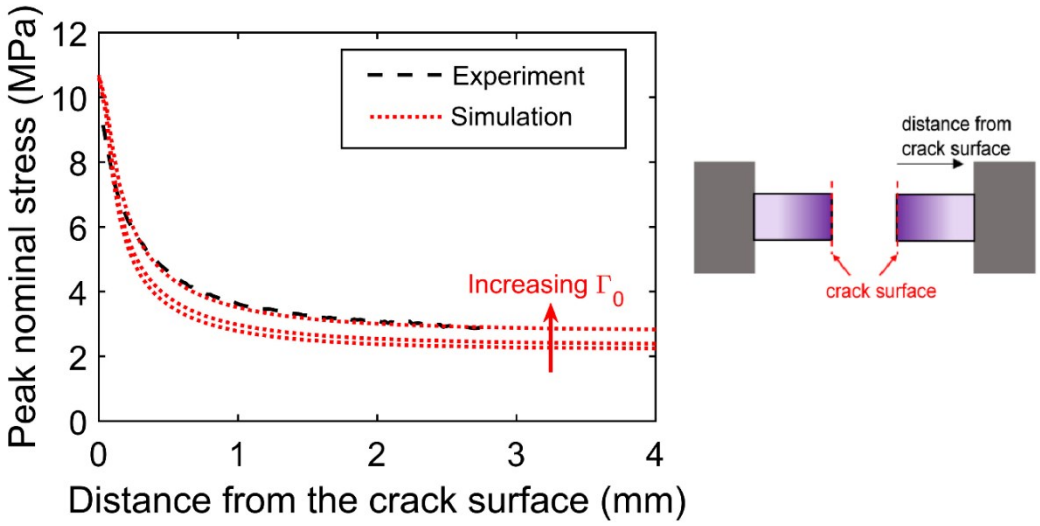

Figure S 23: *Comparison between the experimental data of peak nominal stress distribution and simulation results based on three different Γ_0 (= 3.46 kJ/m², 3.77 kJ/m², 4.6 kJ/m²) and the same σ_{c_max} (= 11.3 MPa). The inset on the right shows a schematic of a completely fractured SEN sample and how the distance from the crack surface was defined.*

Second, Γ_0 was determined by fitting the peak nominal stress distribution obtained from the post-mortem analysis. Specifically, we ran FE simulations using different values of Γ_0 and extracted the peak nominal stress from each simulation. As demonstrated in our previous work[2], the experimentally measured nominal stress should be interpreted as the maximum principal nominal stress, which is equal to the maximum principal true divided by the corresponding principal stretch ratio. Following this definition, we calculated the maximum principal nominal stress and recorded its peak value along the deformation history, which was referred to as the "peak nominal stress". To compare with the post-mortem data, we extracted the peak nominal stress along 7 vertical paths located at 0.5 mm, 1mm, 1.5 mm, 2 mm, 2.5 mm, 3 mm, or 3.5 mm ahead of the original crack tip, respectively. Average of the peak nominal stress was plotted in Fig. S23 together with experimental data from the post-mortem analysis, showing that the case of $\Gamma_0 = 4.6$ kJ/m² produced an excellent agreement with the experimental data. Using $\sigma_{c\_max} = 10$ MPa and $\Gamma_0 = 4.6$ kJ/m², we

computed the contours of peak nominal stress and the distributions of peak nominal stress and energy densities (i.e. total, elastic and dissipated) in after complete propagation, and plotted them in Fig. 5 of the main text. The energy densities were calculated assuming each material point experienced cyclic uniaxial tension during crack propagation, i.e. neglecting the effect of multi-axial deformation state near the crack tip. The shaded regions for the simulations in Fig. 5b and Fig. 5c represent the range of results on the selected 7 vertical paths.

The value Γ_0 = 4.6 kJ/m^2 can be further justified. It is seen from Fig. 3c of the main text that the onset of catastrophic crack propagation for EA0.2-0.05(2.61) occurred at λ = 2.32. For SEN sample, the energy release rate G at a certain global stretch ratio λ can be calculated using the following equation[11-12]:

$$G = \frac{6}{\sqrt{\lambda}} \psi(\lambda) c, \qquad \text{(S11)}$$

where c = 1mm is the initial crack length and $\psi(\lambda)$ is the work per unit volume required to stretch the material to λ under uniaxial tension. Using our constitutive model which provided an excellent fit to the loading curve (see Fig. S22), we found that $\psi(\lambda = 2.32) = 1.015\times10^6$ J/m^3 by integrating the area underneath the uniaxial stress-stretch curve of loading. Plugging this value into Eq. (S11), we obtained that G = 4 kJ/m^2 at the onset of catastrophic crack propagation, which is close to the fitted value of Γ_0 = 4.6 kJ/m^2. Strictly speaking, since bulk dissipation can further enhance the fracture energy in addition to Γ_0 [9-10], 4 kJ/m^2 should be interpreted as an upper bound for Γ_0 and yet it is ~13% smaller than the fitted value of Γ_0 = 4.6 kJ/m^2. To explain this discrepancy, we note that Eq. (S11) was obtained for rubber obeying the Mooney-Rivlin or the neo-Hookean model[12-13]. However, the EA0.2-0.05(2.61) elastomer exhibited a strong strain stiffening behavior (see Fig. S22b), implying that a correction factor may be needed in the application of Eq. (11) to our experiment.

5.4 Simulated stress maps

In Fig. S24, we plotted the global nominal stress versus stretch ratio curve obtained from the simulation. Also included were the simulated stress maps at 6 different stretch ratios, which well captured the unloading regions featured in Fig. 3c of the main text. Despite the excellent agreement between simulation results and the post-mortem data (see Fig. 5 of the main text), the FE model

slightly overestimated the stress and stretch at the onset of catastrophic crack propagation. This is attributed to the possible difference in the crack tip geometry: our model assumed an ideal 2D crack, while in the experiment non-ideal crack tip geometry (e.g. slightly tilted crack front or micro-branches at the initial crack tip) may result from the cutting process that introduced the crack.

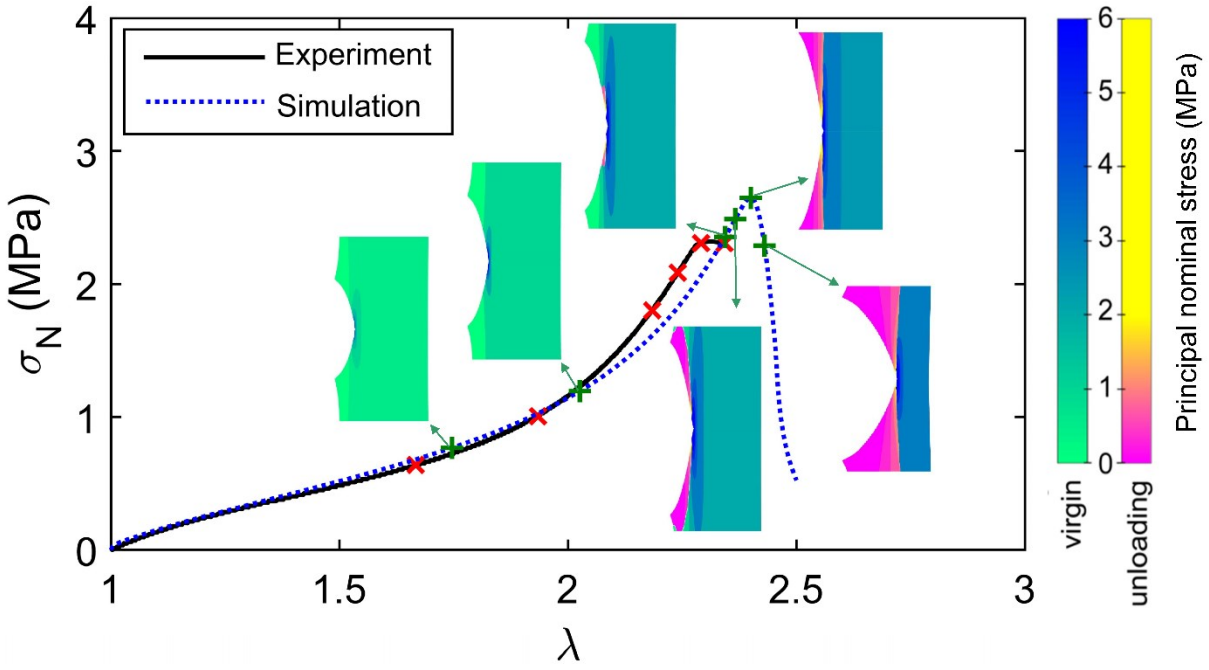

Figure S 24: *Global nominal stress sN versus l for the SEN sample. The blue dotted line is obtained by the simulation and the black solid line represents the experimental data. Also included are the simulated stress maps corresponding to green symbols ("+") on the simulated stress-stretch curves. The red symbols ("x") on the experimental curve mark the points corresponding to the measured stress maps in Fig.3c of the main text (not shown here).*

References

1. G. O'Bryan, B. M. Wong, J. R. McElhanon, Stress sensing in polycaprolactone films via an embedded photochromic compound. *ACS applied materials & interfaces* **2010,** *2* (6),1594-600.(10.1021/am100050v)

2. Y. Chen, C. J. Yeh, Y. Qi, R. Long, C. Creton, From force-responsive molecules to quantifying and mapping stresses in soft materials. *Science advances* **2020,** *6*,eaaz5093

3. M. Bacca, C. Creton, R. M. McMeeking, A Model for the Mullins Effect in Multinetwork Elastomers. *Journal of Applied Mechanics* **2017,** *84* (12).(10.1115/1.4037881)
4. X. Wang, W. Hong, Pseudo-elasticity of a double network gel. *Soft Matter* **2011,** *7* (18).(10.1039/c1sm05787a)
5. X. Zhao, A theory for large deformation and damage of interpenetrating polymer networks. *Journal of the Mechanics and Physics of Solids* **2012,** *60* (2),319-332.(10.1016/j.jmps.2011.10.005)
6. C. O. Horgan, R. W. Ogden, G. Saccomandi, A theory of stress softening of elastomers based on finite chain extensibility. *Proc. R. Soc. Lond. A* **2004,** *460*,1737-1754
7. E. M. Arruda, M. C. Boyce, A three-dimensional constitutive model for the large stretch behavior of rubber elastic materials. *J. Mech. Phys. Solids* **1993,** *41*,389-412
8. A. Cohen, A Padé approximant to the inverse Langevin function. *Rheol Acta* **1991,** *30*,270-273
9. Y. Qi, J. Caillard, R. Long, Fracture toughness of soft materials with rate-independent hysteresis. *Journal of the Mechanics and Physics of Solids* **2018,** *118*,341-364.(10.1016/j.jmps.2018.05.020)
10. T. Zhang, S. Lin, H. Yuk, X. Zhao, Predicting fracture energies and crack-tip fields of soft tough materials. *Extreme Mechanics Letters* **2015,** *4*,1-8.(10.1016/j.eml.2015.07.007)
11. A. Cristiano, A. Marcellan, B. J. Keestra, P. Steeman, C. Creton, Fracture of model polyurethane elastomeric networks. *Journal of Polymer Science Part B: Polymer Physics* **2011,** *49* (5),355-367.(10.1002/polb.22186)
12. H. W. Greensmith, Rupture of rubber. X. The change in stored energy on making a small cut in a test piece held in simple extension. *Journal of Applied Polymer Science* **1963,** *7*,993-1002
13. O. H. Yeoh, Relation between crack surface displacements and strain energy release rate in thin rubber sheets. *Mechanics of Materials* **2002,** *34* (8),459-474